communications materials

A Nature Portfolio journal

Article

https://doi.org/10.1038/s43246-025-00993-y

Manufacturing planar perovskite solar cells in dusty environments

Kathryn Lacey[1], Ershad Parvazian[1], Sarah-Jane Potts[1], Tom Dunlop[2], James McGettrick[1], Krishna Seunarine[1], Eifion Jewell[1], Matthew Davies[1], Matt Carnie[1] & Trystan Watson[1]

Production of silicon solar cells necessitates cleanrooms to prevent dust contamination, which can lead to defects and reduced performance. This poses challenges for scaling up manufacturing and improving accessibility for device manufacture in less developed economies as cleanrooms represent an expensive and energy intensive investment, and so it is key that the next generation of solar technology differentiates from this. Perovskite has the potential to be far more robust and resilient to defects caused by dust particles, which then impacts on the capital cost of the equipment required for manufacture. This study evaluates the effects of non-conductive dust on planar perovskite devices, testing two different device structures with efficiencies exceeding 16%, testing an active area of 0.09 cm^2. The setup simulated dust settling during the manufacturing process, expecting compromised performance in contaminated devices. Results revealed that devices with dust performed similarly to clean ones, with only limited losses in some performance metrics. High tolerance to contamination suggests that perovskite technology may remain operational under less controlled environments. These findings point toward a more accessible fabrication route reducing dependence on expensive cleanroom conditions typically required for silicon-based technologies.

Perovskite solar cells (PSCs) present a strong opportunity to make renewable energy more accessible than ever, with continually increasing efficiencies being recorded, the low cost of materials required and relative ease of manufacture in comparison to the current most widely used material silicon. Lead halide PSCs are currently achieving power conversion efficiencies of up to 26%[1], with a high potential intrinsic efficiency limit of ~30.5%[2].

Defects in perovskite films range from a single atom out of place in the crystal structure, to larger scale microstructure interruptions. These changes can affect the transport and excitation of charge in a PSC[3]. Defects can cause traps which can result in the unwanted recombinations of charge carriers. Most traps present in lead halide perovskite films are shallow[4,5] and do not generally impact on the performance of a PSC[3,6], but deep traps can also occur which may impact on PSC performance[7].

In a planar device perovskite solution is deposited to create a thin film around 400–700 nm in thickness. The ideal metal halide perovskite film has large, regular crystals with lateral growth, which results in the highest performing devices[8]. Presence of a dust particle on a micron scale has the potential to cause interruptions or differences to the formation of perovskite crystals and microstructure, acting either as a nucleus or a separate surface for unanticipated direction and size of crystal growth. Surface energy is a key driver for crystal growth size and direction, and a particulate of different material may have a different surface energy to the surrounding area, causing suboptimal crystal growth[9] and continuation of this over a larger area. There is also the potential for the presence of larger particulates to break up or interrupt the crystal microstructure across the perovskite film, which may result in increased variation in crystal size and more grain boundaries, both of which are associated with deeper traps causing more carrier losses and nonradiative recombinations[10,11]. While shallow traps near the band edges may temporarily delay charge transport without major efficiency losses, deep traps act as non-radiative recombination centres, permanently capturing carriers and reducing photocurrent and fill factor. Such traps are often associated with grain boundaries or interfacial defects—conditions that may arise from dust-induced microstructural disruption.

Dust particles may also result in a rougher surface interface, which can cause more complexities in PSCs with the roughness of the layer below dictating the grain size formation of the perovskite layer deposited onto it - smoother surfaces allow larger and more homogenous perovskite crystals to form[12]. Interfaces are a significant area of deep traps in PSCs[13]. A smoother interface also allows the deposition of thinner, more homogenous layers promoting improved charge extraction and less material use and reduces the

[1]Specific Ikc, Faculty of Science & Engineering, Swansea University, Swansea, UK. [2]Aim, Faculty of Science & Engineering, Swansea University, Swansea, UK. e-mail: t.m.watson@swansea.ac.uk

risk of pinholes which may contribute to a variety of problems including electrical shorts, reduced active area and faster degradation of a device[14–16].

Lab-scale PSCs are therefore typically made in a cleanroom environment to limit interaction with any dust in the atmosphere. This is a manufacturing process informed by established standards in the semiconductor industry, including silicon semiconductor wafers[17] which are already known to be susceptible to damage during manufacture from dust particles present in the atmosphere[18,19]. As the layers become thinner with increased efficiencies of the materials, presence of dust particulates can become more of a problem. Deposition of thin, nanometre scale layers of semiconductor materials to create a high efficiency PSC would therefore be considered to require a clean, particle-free environment, as any defects caused by particles may disrupt layer quality and reduce overall functionality. However, cleanrooms create a significant cost and infrastructure barrier and use considerable amounts of energy[20]. Because of this many industries look towards making manufacture more accessible by investigating ways to reduce or eliminate the need for them[21–23,] As one of the main advantages of PSCs is their low cost of manufacture in terms of materials, the cost of what is required for the setup of suitable manufacturing environment is also important to consider, both for less developed economies and for the upscaling of PSC manufacture.

To date, very little research has gone into quantifying precisely how dust particles present during manufacture affect the performance of a PSC. It is important to understand the number and nature of these defects. This study will aim to compare and analyse lab scale devices made in a cleanroom environment with those from the same batch placed purposely into a controlled dusty environment, to consider how particles in the atmosphere impact on PSCs. Device structures have been chosen to provide data for both a classical device structure and looking forward to a scalable structure using carbon. This latter configuration not only ensures reproducibility and facilitates the production of comparable batches of devices, but it also constitutes a roll-to-roll (R2R) compatible stack. This is particularly relevant as R2R production is typically conducted in open spaces where environmental factors such as dust have a more pronounced impact compared to controlled conditions, such as within a fume hood. Thus, the findings of this study can also be helpful for research focused on roll-to-roll fabrication of perovskite devices. Ultimately, are cleanrooms a requirement for the manufacture of high performing PSCs? In this work, high performing PSCs are presented on the basis of their environmental manufacturing conditions of an ambient environment using scalable processes, and so upper efficiency limits are somewhat constrained to 17%. To this end the impact of dust on a > 25% device is not investigated.

If a controlled cleanroom environment is not essential, this means far more accessible manufacturing and the potential for re-purposing existing infrastructure rather than needing to foot significant costs to install and maintain more.

Results and discussion

To investigate the impact of dust particles on device performance, we designed experiments delivering the controlled deposition of quantifiable dust particles at varying interfaces, between layer depositions. This process involved two critical control considerations: identifying a suitable proxy for atmospheric particles and establishing a reliable method for monitoring to ensure reproducibility.

Characterising dust

An industry standard test dust was chosen for use in these experiments. This manufactured dust is primarily designed for testing the effectiveness of air filtration devices. The material type used for testing was a cotton fibre dust, the purpose being to assess the physical impact of the presence of a non-conductive foreign particle. The test dust contained a particle size range comparable to cleanroom standards, ~90% by volume below 5 µm. The particle size ranges are analogous to the smallest particles in the air tested for in a cleanroom. Experimental results can be placed in context of cleanrooms up to an ISO class 3 cleanroom where particle sizes only have an allowance of up to 5 µm under the ISO 14644-1 cleanroom standard classifications (382.59 ≥ 5 µm per m^3 of air).

Figure 1a, b shows characterisation of the dust in both size and roundness, respectively. The distribution of both size and shape shows a reasonable match across all areas in comparison to the test dust. Samples for imaging were acquired by leaving sticky carbon tabs in each location for several days, which could then be used directly for SEM imaging. Images of dust particles from the standard lab and the class 7 cleanroom also showed a reasonable visual match for both size and shape to the test dust samples (Fig. 1c), and although chemical analysis revealed a few extra elements detected in some particles, many were found to be likely organic in nature with only small traces of conductive materials. In general, the test dust provides a suitable parallel to many dust particles found in the labs.

Samples of dust were taken from multiple areas around materials science labs at Bay Campus, Swansea University. Swansea University is located in a coastal region of the northern hemisphere and experiences a temperate maritime climate. Lab dust samples included an ISO class 6 cleanroom, ISO class 7 cleanroom, inside a fume hood in a standard lab, and the middle of a standard lab. In this context, a standard lab means where open benches and fume hoods are used, and no special controls on the environment exist aside from air conditioning. Samples for the particle size and shape analyser were taken from the work surfaces of each area to obtain a sufficient sample set.

Dust box experiment setup

Creating an enclosed environment for distributing dust over samples was important in order to represent an accelerated version of conventional settled dust. There was also a requirement of monitoring the volume of particulates being circulated to assess for reproducibility of the amount of dust and the time that dust was circulated for. A box was designed to fulfil this purpose (Fig. 2a). Dust was weighed out to ensure consistency and placed into the base of the box, then circulated via airflow into the base of the box where it would not disturb the devices on the sample platform. The number of particles between 0.1 and 10µm circulated in the box was recorded.

Figure 2b shows the predicted dust particle drop-out rate per hour from the atmosphere onto a centimetre square surface vs. atmosphere particle count in locations including standard laboratories, a fume hood in a standard laboratory, nearby building corridors and clean rooms of class 6 and 7. These figures were calculated based on the average density of the test dust at 0.45 g/cm^3, highest frequency dust particle radius of 1 µm zero flow rate and zero air turbulence. Particle drop-out rates are placed in comparison with similarly calculated rates using particle counts from inside the dust box when test dust was circulated. To place this in a real-world context, Fig. 2c shows the equivalent number of hours for a sample to sit in each location required to match the dust circulated onto samples within the dust box. In standard laboratories and corridor areas the dust box value is representative of between 24 and 66 hours of a device standing collecting dust. In both clean rooms this figure extended considerably to between 1412 h (58 days) in a class 7 clean room up to 8864 h (370 days) in a class 6 clean room.

The quantity of dust circulated in the dust box allowed a uniform distribution of dust particles across devices, ensuring sufficient deposition to enhance the likelihood of observing changes induced by individual particles, as well as potentially revealing immediate impacts on device performance.

Device samples were left in the box to passively collect settling particles as the dust was circulated. Control samples were made in a class 7 cleanroom where prior to the next layer deposition any dust particles were removed from the sample with a small air blower. Where it is mentioned that dust is at a specified layer (for example, after the SnO_2 deposition and annealing, but before perovskite deposition), test dust was circulated and settled onto the sample *before* that layer was deposited. These exposure durations were intentionally designed to represent accelerated contamination scenarios. While actual fabrication of a full device in our process takes less than 120 min, the short dust exposure in the test box (~ 3 min) was equivalent to

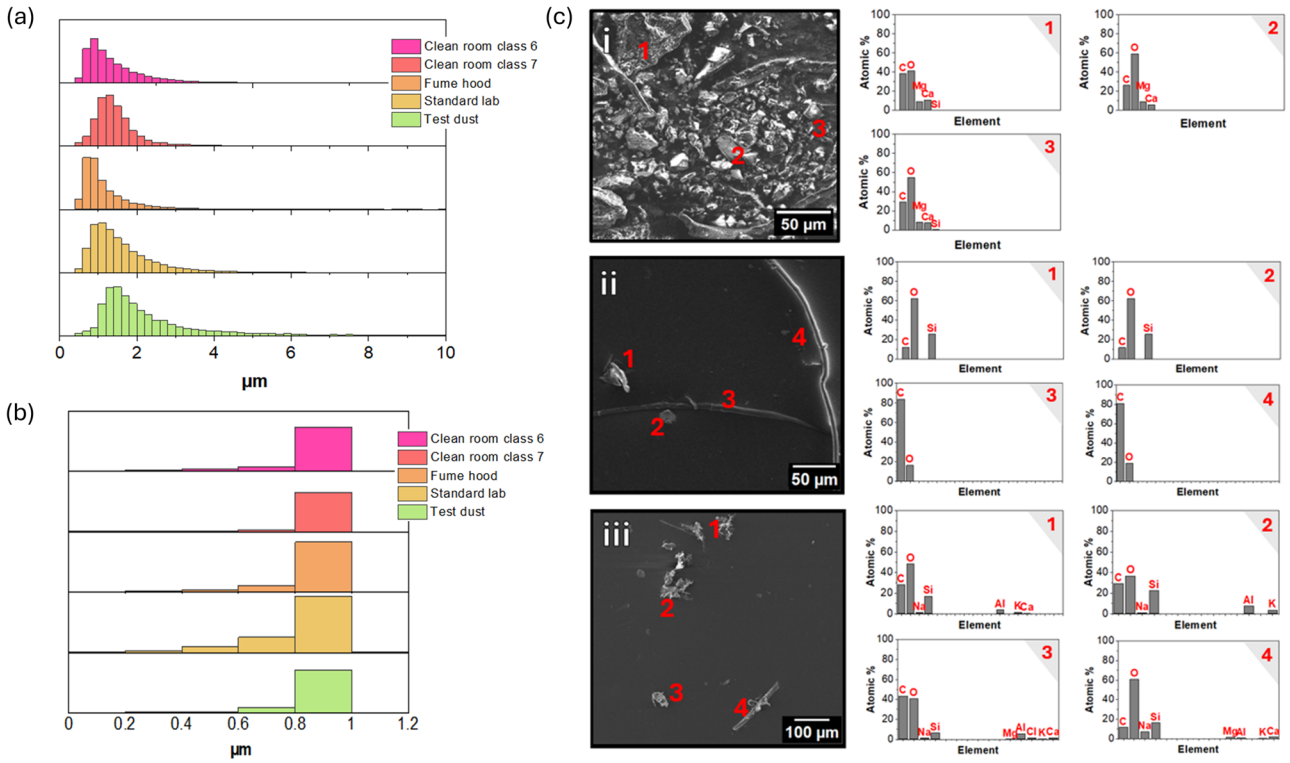

Fig. 1 | Dust particle size, morphology and chemistry characterisation. a particle size analysis for varying laboratory environments; (**b**) particle roundness analysis for varying laboratory environments; (**c**) SEM images and EDS results from (i) sample of test dust, (ii) standard laboratory, and (iii) ISO class 7 cleanroom.

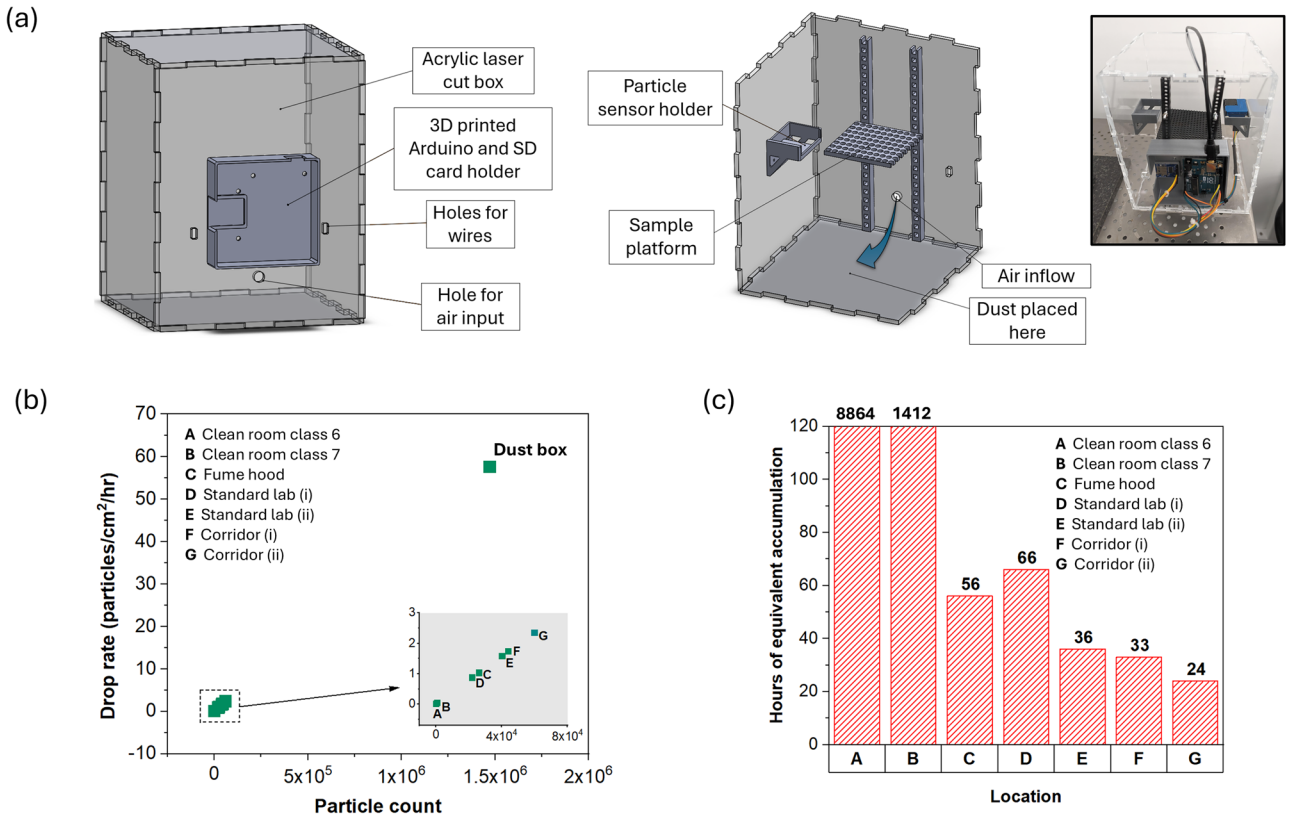

Fig. 2 | Design, setup and context of dust box experiment. a outside and inside schematics of dust box alongside photograph of final dust box setup; (**b**) scatter graph of particle drop-out rate vs. particle count in different areas compared with dust box; (**c**) bar graph of the hours of dust particle accumulation the dust box circulation is equivalent to in each area.

weeks or even months of passive dust accumulation under real-world conditions, depending on the cleanliness level. This approach ensures that any potential impact of dust—especially at specific fabrication stages—is exaggerated enough to reveal even subtle performance losses, thereby highlighting whether strict cleanroom environments are indeed necessary for maintaining device quality.

Dust impact on planar devices

Tests were run on two different types of commonly used planar device stack (Fig. 3a). The first represented a scalable device for roll-to-roll (R2R) production incorporating a printed carbon electrode[24]. R2R scalable devices are an important consideration as the purpose of this study is to consider the upscaling process and what is required for this alongside innovations in the process itself[25]. This stack consists of an NIP structure with an ITO substrate, tin oxide for the ETL, MAPI perovskite, PEDOT for the HTL and carbon for the top contacts. All are thin film deposited, and scalable to print R2R.

The second device stack is a more typical lab device often used to test changes to materials to achieve higher efficiency devices. Also, an NIP structure, in this instance the whole device remains the same up to the HTL layer where Spiro-MeOTAD is used, and gold contacts are evaporated instead of printing carbon contacts.

R2R scalable devices (PEDOT/carbon). The first set of experiments assessed how dust impacted the deposition of layers on SnO_2/MAPI/PEDOT/carbon devices scalable for R2R production. Four sets of R2R compatible devices were made: control samples with no dust particles, dust before SnO_2 (ETL) deposition, dust before MAPI deposition, and dust before PEDOT (HTL) deposition. The previous layer was fully annealed as appropriate on the hot plate prior to any dust deposition.

The first set of devices and samples compared clean controls with those with dust deposited prior to the SnO_2 TL layer. Photographs were taken of devices after dust deposition to note proof of the dust presence (Fig. 3b). The amount of dust circulated was recorded to an SD card (Fig. 3c) to verify that between sample sets there was a similar amount deposited ($< 500\ \mu g/m^3$). Devices and samples were then tested and characterised to see whether there were any differences in the function of control vs. dusty samples.

JV testing of completed devices showed some differences in the function of control devices vs. those following dust deposition at the SnO_2 layer, with a reduction in PCE evident. This was resultant from a small reduction in both FF and J_{sc} (Fig. 3f)—a larger variability was also evident in J_{sc}. A difference was also evident in the spin coated layers shown via electroluminescence (EL) mapping (Fig. 3d) where dust particles and changes in the layers can be seen, due to reduced EL in these locations. Reduced EL is only seen at the spots where a dust particle itself present, showing that these are inactive areas where there is no SnO_2.

To determine the blocking function of the SnO_2 layer, cyclic voltammetry was performed on bare ITO, the control sample with clean SnO_2 and dusty SnO_2 (Fig. 3e). This was to assess whether the presence of dust particles may cause pinholes in the ETL layer, as pinholes in the ETL of a complete device may result in electrical shorts. As expected, the bare ITO showed good conductivity. Notably, both the control and dusty samples gave identical results, indicating a strong blocking function from both.

The next set of devices and samples compared clean devices with those with dust deposited prior to the MAPI layer deposition.

SEM images were taken to observe dust particles and whether there were any changes in the perovskite crystallisation (Fig. 4a). For the most part, the presence of dust particles did not appear to alter the crystallisation, however, a change in thickness near dust particles was noted. AFM scans

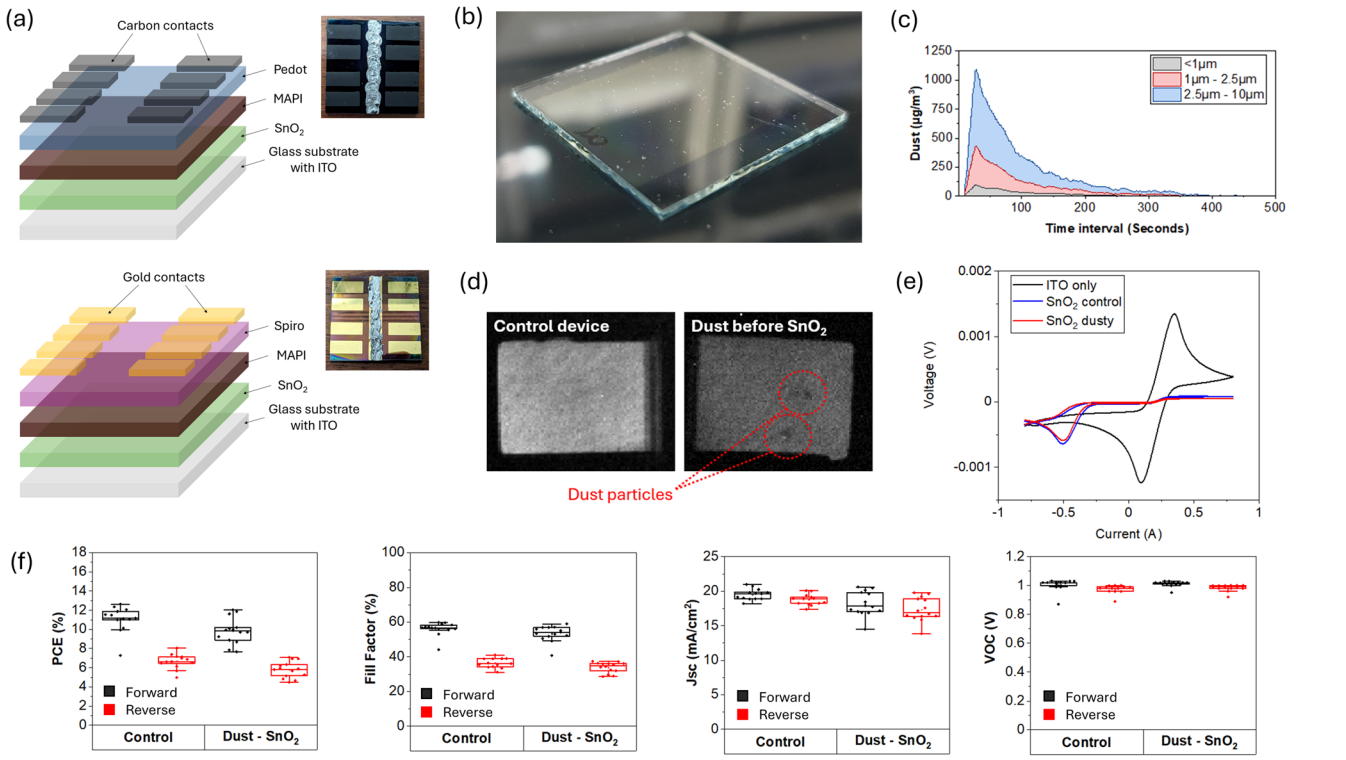

Fig. 3 | Device stack introduction alongside electroluminescence (EL) mapping, cyclic voltammetry and JV results from R2R compatible stack control devices vs. devices with dust deposited before the SnO_2 layer. a Device stack schematics – R2R compatible stack (carbon) and standard lab stack (gold); (**b**) photo showing evidence of test dust deposited onto a glass/ITO substrate prior to SnO_2 deposition; (**c**) output of dust particle measured while depositing dust onto substrates; (**d**) EL mapping of single pixels from completed devices, control samples and those with dust deposited prior to SnO_2 deposition; (**e**) cyclic voltammetry comparing clean glass/ITO substrates, substrates with clean SnO_2 deposited on top, and substrates with dust then SnO_2 deposited on top; (**f**) PCE, fill factor, J_{sc} and V_{oc} boxplots of control samples vs. those with dust prior to SnO_2.

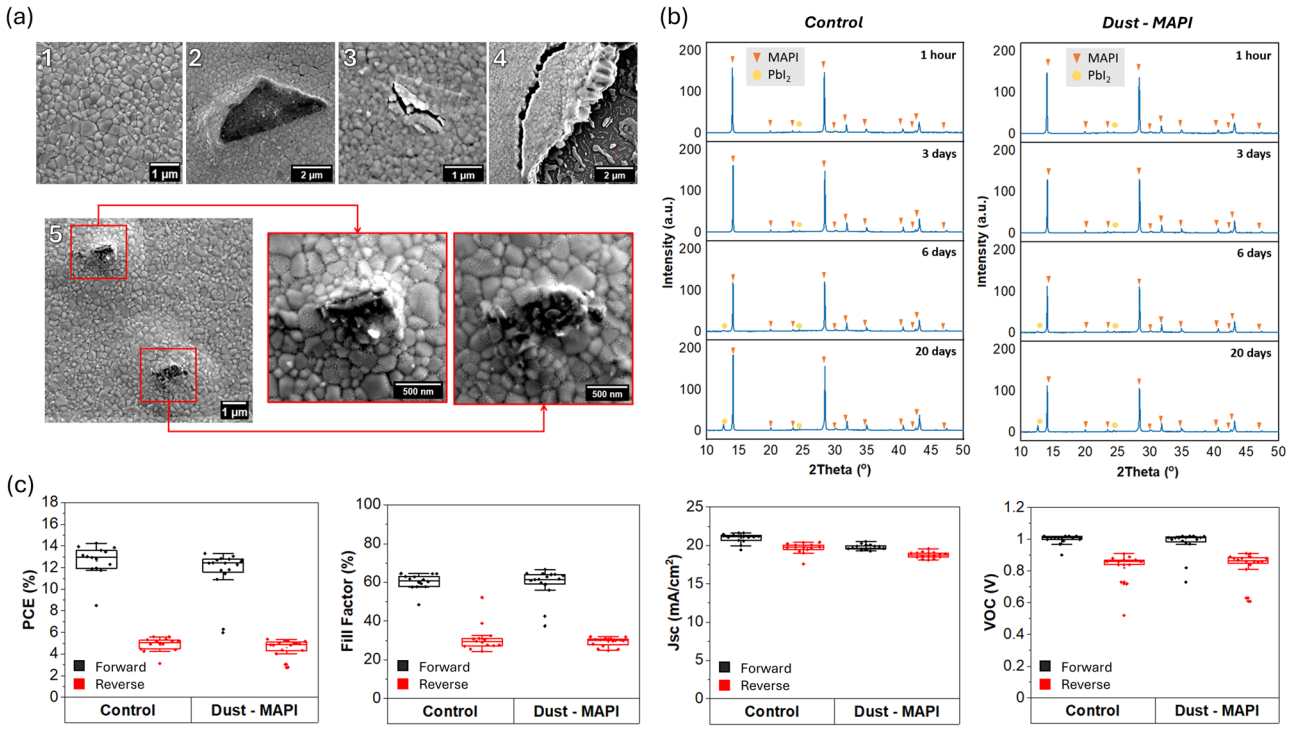

Fig. 4 | SEM, XRD and JV results for R2R compatible control devices alongside devices with dust deposited before the MAPI layer. a SEM images of perovskite crystals: (1) clean control sample, (2) dust particle, (3) break in perovskite crystal microstructure, (4) edge of break in perovskite microstructure showing SnO_2 underneath, (5) two dust particles in perovskite microstructure with focus on each; (**b**) XRD data comparing control to dusty MAPI samples over a number of days; (**c**) PCE, fill factor, J_{sc} and V_{oc} boxplots of control samples vs. those with dust deposited prior to MAPI deposition.

revealed this to be a thinning of the perovskite film in the direction of spin coating (supplementary Fig. S1).

Crystals remained much the same size and shape, with no evidence to show that particles had provided a different surface energy to change the morphology of crystals. Some particles caused breakages in the crystal microstructure, and others changed the roughness of the topography near the dust particle. On some occasions, gaps in the crystal microstructure could be seen where it was suspected that a dust particle had been deposited but was dislodged after the perovskite crystallisation had taken place. Most dust particles appeared to remain in place despite the spin coating process, with perovskite crystals forming around and over them with no change to the crystal size or shape. This suggests that perovskite crystal formation is resistant to changes when a non-conductive particle is present. Breakages in the microstructure may sometimes occur and the topography of the microstructure may alter to a degree, but aside from this the perovskite layer forms normally.

To determine whether contaminants within the dust particles located under the perovskite accelerated or resulted in any additional degradation pathways, XRD analysis was used to assess any differences in the degradation of the MAPI to lead iodide between control and dusty samples over time up to 20 days. XRD was carried out on the samples an hour after production, 3 days, 6 days and 20 days (Fig. 4b). No notable difference was observed in how the MAPI degrades to lead iodide in either sample, both appeared to degrade at the same rate with no unexpected peaks were noted, only those of MAPI/lead iodide with no indication of phase splitting and lead iodide only noticeable degradation product. All peak positions within the expected for MAPI (refs) with no noticeable shifts in microstructure parameters indicating no structural change with the addition of dust and during degradation process.

Additional XRD and photoluminescence (PL) mapping analyses were performed on both control and dust-contaminated MAPI films, under fresh and thermally aged conditions, to evaluate degradation over 100 h of thermal treatment at different temperatures: one at 65 °C and another at a more elevated temperature of 85 °C representing a harsher environment. In both thermal conditions, the control and dust-containing films showed comparable perovskite degradation behaviour, indicating that dust did not exert a considerable destabilising effect on the perovskite (supplementary Figs. S2 and S3).

Figure 4c shows the results of the JV analysis. Dusty devices showed a slightly lower PCE, alongside a drop in J_{sc}. V_{oc} and FF were unaffected.

The final stage of R2R compatible devices tackles the influence of dust on the HTL. The analysis compared clean devices with those with dust deposited prior to PEDOT (HTL) layer deposition.

To see at the nanoscale whether differences could be seen in the PEDOT, SEM images were captured of any changes likely to be caused by dust (Fig. 5a). PEDOT is an amorphous polymer which is difficult to image by SEM and often the layer below (MAPI) underneath is imaged. Due to this limitation only areas where there were breakages could be seen clearly enough, and it was not always certain that this could be attributed to dust particles. In very few instances, it appeared likely that a particle had been present but subsequently lost from the PEDOT after annealing (1 & 2). In other instances, a disturbance to the uniformity of the PEDOT layer could be due to a particle underneath it; image 4 highlights a bubble in the PEDOT, and next to it a particle can be seen underneath the PEDOT layer. Despite being clearly visually present in optical microscopy, under the SEM none of these comet-like structures could be visualised, suggesting that the disruptions to the layer were on the whole not breakages but changes in surface topography difficult to detect via SEM, as was previously confirmed by AFM scans of dust in the MAPI layer.

Particles were certainly left behind underneath the layer after spin coating, as was also evidenced by the EL mapping (Fig. 5b) which clearly showed the comet-like distortions in PEDOT deposition caused by the presence of dust particles underneath, the dark point showing reduced EL due to a non-conductive presence (dust particle) and the brighter streaks outwards from these suggesting again a difference in layer thickness of the PEDOT behind it in the direction of deposition.

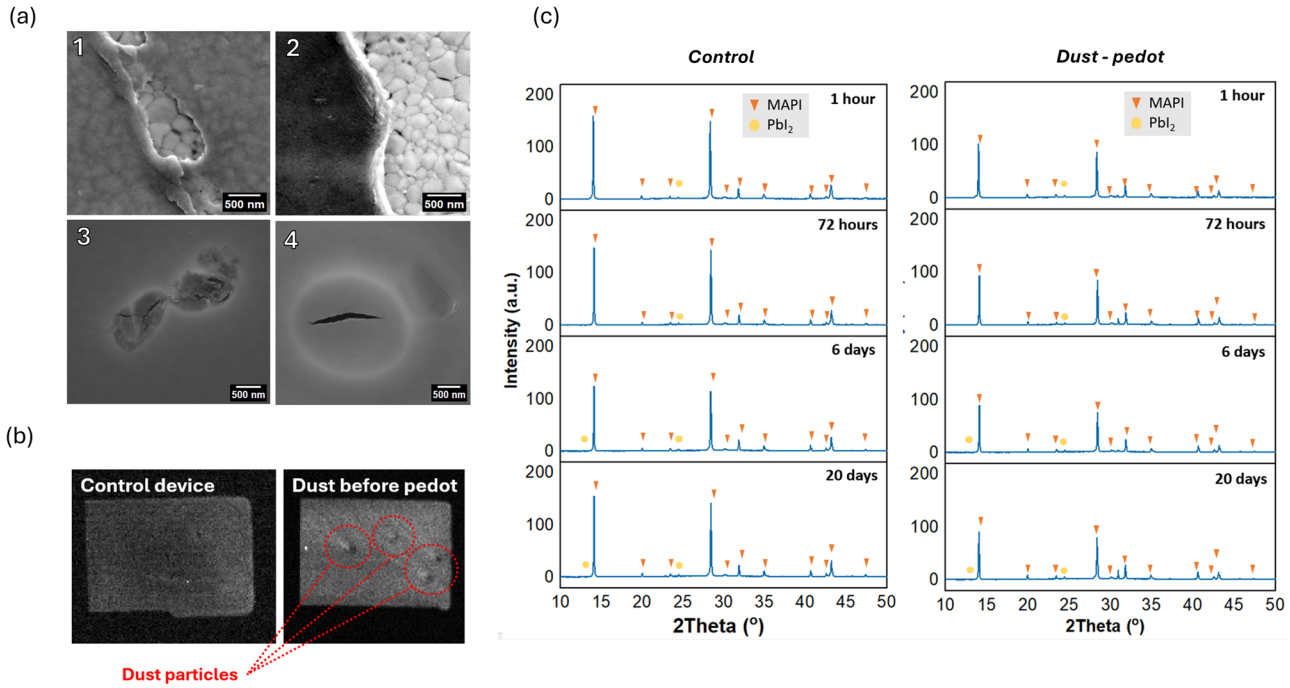

Fig. 5 | SEM, EL mapping and XRD results of R2R compatible control devices alongside devices with dust deposited before the PEDOT layer. a SEM images of dust damage to PEDOT; (**b**) EL maps showing evidence of changes to PEDOT with dust particle presence; (**c**) XRD data comparing control to dusty PEDOT samples over a number of days.

XRD was also applied to these samples for differences with the degradation from MAPI to lead iodide (Fig. 5c). Control samples and those with dust in between the perovskite and PEDOT layers were tested an hour after production, 3 days, 6 days and 20 days. Again, no difference was noted, showing that the dust particles still did not contribute to any additional or accelerated pathways, and no further interactions resulting in any degradation were introduced with the solvents in the PEDOT deposited over top of the dust particles.

Figure 6a shows the optical microscopy comparison of control samples with dusty samples. The data showed that it was evident that on the dusty samples there were some disturbances in the deposition of the PEDOT layer in the form of comet-like structures radiating out from the centre of the device and occurring at all points across the sample showing that dust at the PEDOT layer causes a similar change in the topography as was seen at the MAPI layer. These could be observed clearly under optical microscopy with particles of all sizes causing disturbances in the PEDOT in front of and behind the particle, resulting in the comet-like structures. On the control sample the PEDOT deposition streaks outwards from the centre of the device with no interruptions, the streaks being an artifact of spin coating deposition.

XPS was carried out on both control samples and samples with dust at the PEDOT layer, focused on the presence of carbon, lead, iodide, nitrogen and oxygen to indicate the MAPI, with the addition of sulfur to examine the PEDOT layers. The peaks and ratios of each element were analysed to identify chemical changes in the vicinity of the dust particles. Map data was created for both the control and dusty PEDOT samples (Fig. 6b). Point scans were also targeted at specific areas where apparent defects were visible—data and images are displayed in the supplementary material as indicated (Fig. S4, Tables ST1, ST2) and includes data for control and dusty MAPI films.

As expected for MAPI films, C, Pb, I, and N were present, with low amounts of oxygen (~ 2 At%) also being observed. Whilst an adventitious carbon shoulder is present at 284.8 eV, the carbon is dominated by the MAPI carbon at 286.3 eV. The primary nitrogen peak is at 402.2 eV, slightly higher than the ~400 eV for organic nitrogen, due to the localisation of positive charge on the nitrogen atom in the MAPI. Pb is present as Pb(II).

Similarly, for the PEDOT films, there was remarkable consistency across 196 points on both the control and dusty samples (supplementary Fig. S5, Table ST3). C, O & S dominate as expected from PEDOT, with low levels of Pb (~ 0.2 At%) and I (0.5 At%) indicating some level of defects—however, these low Pb & I signals were observed consistently at all points on both samples. For the PEDOT, there are two distinct sulfur peaks: oxidised sulfonate and the lower binding energy PEDOT sulfur. Again, these were monitored for variation that might indicate a change in chemistry and were shown to be consistent within a sample.

The iodine, lead and carbon maps show device-scale spatial distribution from the centre to the edge of all devices where higher counts were detected for these elements towards the centre. This is normal variation due to the nature of spin coating deposition. Some variances of these elements from the expected ratio are present simply due to surface contamination adding a small quantity detected to C and N, but ultimately there were few differences that could be attributed to changes in chemistry within the sample.

In general, all expected peaks were visible and matched very closely, showing that both the MAPI and PEDOT films completely covered the dust particles and maintained an unbroken layer.

Figure 6c shows the JV data for this batch. Almost no difference between the control and dusty samples can be seen, except for a slightly lower Jsc with the dusty devices. PCE, FF and V_{oc} show little difference (in fact, fill factor could be said as being slightly higher). As we would expect defects reducing layer quality or connectivity to increase the number of traps present, this would also be reflected in a drop in V_{oc} or FF, neither of which are apparent here.

The impact of adding higher levels of dust at each layer of PEDOT/carbon cells was also analysed, including devices with dust at every layer. For devices so far, the amount of dust circulated was kept to <500 μg/m^3. For devices with higher levels of dust this amount was approximately doubled to >1000 μg/m^3.

Dust levels of >1000 μg/m^3 slightly reduced the performance and consistency of these devices (Supplementary Fig. S6), and this result was amplified with dust present at every layer of the device. EL maps confirmed this drop in function with significantly reduced luminescence noted in the

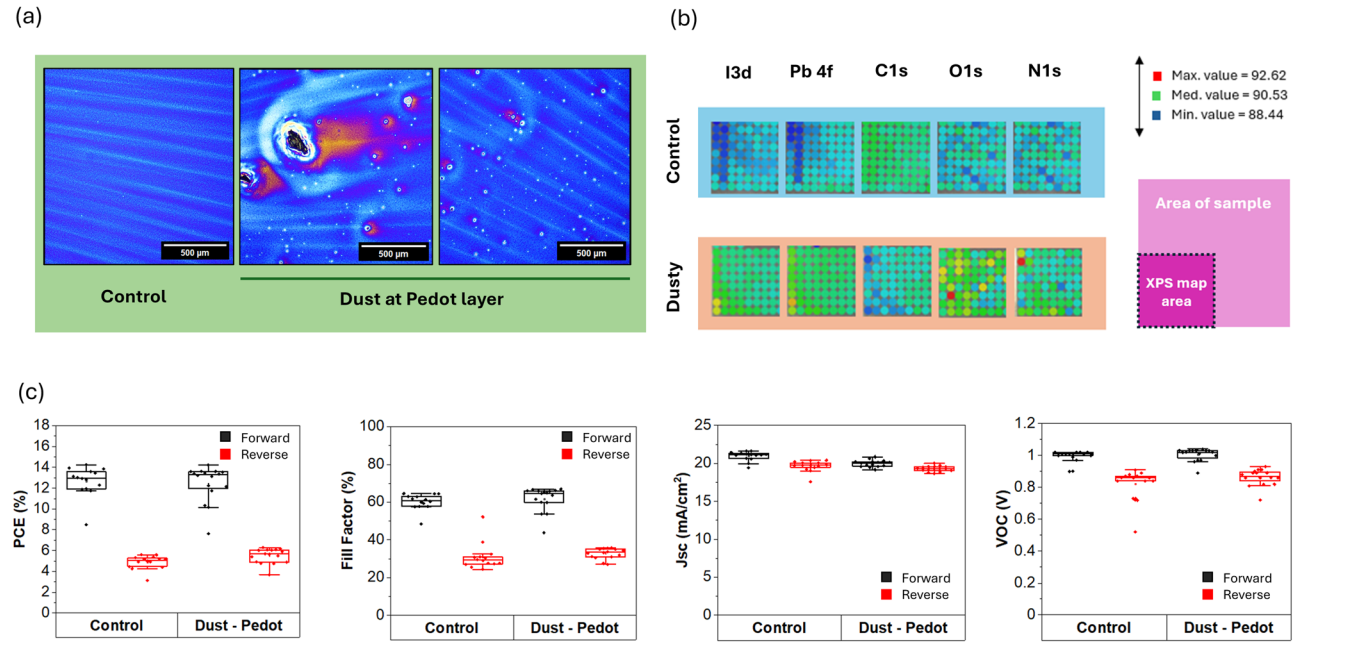

Fig. 6 | Optical images, XPS and JV data of R2R compatible control devices alongside devices with dust deposited before the PEDOT layer. a Optical microscopy comparison of control to dusty samples; (**b**) XPS maps of control sample and dusty PEDOT over top of MAPI; detailing iodine, lead, carbon, oxygen and nitrogen distribution with schematic showing mapped area of each sample; (**c**) PCE, fill factor, Jsc and Voc boxplots of control samples vs. those with dust deposited prior to PEDOT deposition; % differences in PCE across all R2R scalable devices with dust at each SnO_2 MAPI and PEDOT layers.

pixels of devices with >1000 µg/m^3 of dust at every layer (Supplementary Fig. S7). As dust particles are shown to block EL (presence of non-conductive particle) and in thinner and therefore less conductive areas for the EL to drop, it is evidenced that this disruption multiplies with higher dust particle presence, resulting in an overall device-wide drop in EL response.

Standard lab stack (spiro-MeOTAD/gold)

Similar experiments were conducted using the standard lab stack of SnO_2/MAPI/spiro-MeOTAD/gold to consider how dust may impact a different type of device stack. Four groups of devices were made: a control group of clean devices with no dust, devices with dust deposited before the SnO_2 layer, devices with dust deposited before the MAPI layer, and devices with dust deposited before the spiro-MeOTAD layer. Gold contacts were evaporated onto all devices.

Initial device performance data showed differences in the performance of control vs. dusty devices (Fig. 7a). Additional PV performance of devices (JV and EQE) available in Supplementary Fig. 8. Reductions in PCE, FF and J_{sc} are increasingly evident the higher up the stack the dust was located, with the largest difference seen when dust was deposited prior to the spiro-MeOTAD deposition. There was also less consistency of PCE, FF and J_{sc} the higher up the stack the dust was located.

EL mapping was applied to individual pixels of devices from each group (Fig. 7b). Control devices showed more uniform EL. Regular dark patches appeared in all the dusty devices indicating reduced EL, with the presence of dust particles showing up differently depending on which layer the dust was located. Dust before the SnO_2 layer showed most clearly, with reduced EL at dust particle locations (where a non-conductive particle is present) as well as streaking out in the direction of spin coating deposition behind dust particles, creating further areas of reduced EL. As these streaks are thinner than the rest of the film, these areas also likely conduct poorly. Dust deposited before the MAPI layer showed up as regular darker areas which are likely due to the perovskite crystals forming around the dust particles as seen in previous SEM images. Streaking behind dust particles seen in other layers is not seen in the MAPI layer due to the solvent loss and subsequent crystallisation. Dust deposited before the spiro-MeOTAD layer did show some evidence of darker spots with streaks showing behind in the outward direction of spin coating, but this reduction in EL was not as apparent at the spiro-MeOTAD layer as it was at the SnO_2.

Figure 7c compares the percentage change in PCE of dusty devices from each group in each device stack with error bars representing the standard deviation of each sample set. The trend of change in device performance dependant on where the dust is located is different for each stack. The R2R compatible stack showed most performance loss when dust was located at the ETL layer, and this reduced the further up the device the dust was deposited. The standard lab stack however showed the largest performance loss with dust located at the HTL layer.

Spiro-MeOTAD and evaporated gold contacts are thinner than PEDOT and carbon contacts, and so it is likely that the presence of dust particles in the size ranges 1–10 µm may impact more on the performance of devices with dust particles at these thinner layers. This is evident in the difference between the results for the two different device stacks where there was little difference in the function of the R2R devices when dust was located at the HTL layer. In the standard lab stack the most significant difference in devices was with dust at the ETL layer.

Conclusion

A novel experimental design was developed for this project to evaluate the impact of atmospheric dust on perovskite solar cells during production. A custom-designed box facilitated controlled dust circulation and monitoring, which enabled the comparison of clean control samples to those with dust deposited at different stages of the manufacturing process.

Overall, some performance loss was seen with dust particles at most layers in both device stacks. The reduction seen in PCE, FF and J_{sc} in nearly all dusty sample groups suggests that wherever dust particles are located, they contribute to reduced active area of the device – evidenced by the largest differences being present in J_{sc}, impacting directly on the PCE and FF. Dust was confirmed present at all layers where they were expected and changes were observed in layer topography via optical images and EL mapping, with particles causing areas of reduced EL - inactive regions - and disturbed areas of layer deposition behind the particles in the direction of spin coating, causing further reductions in the active area of devices.

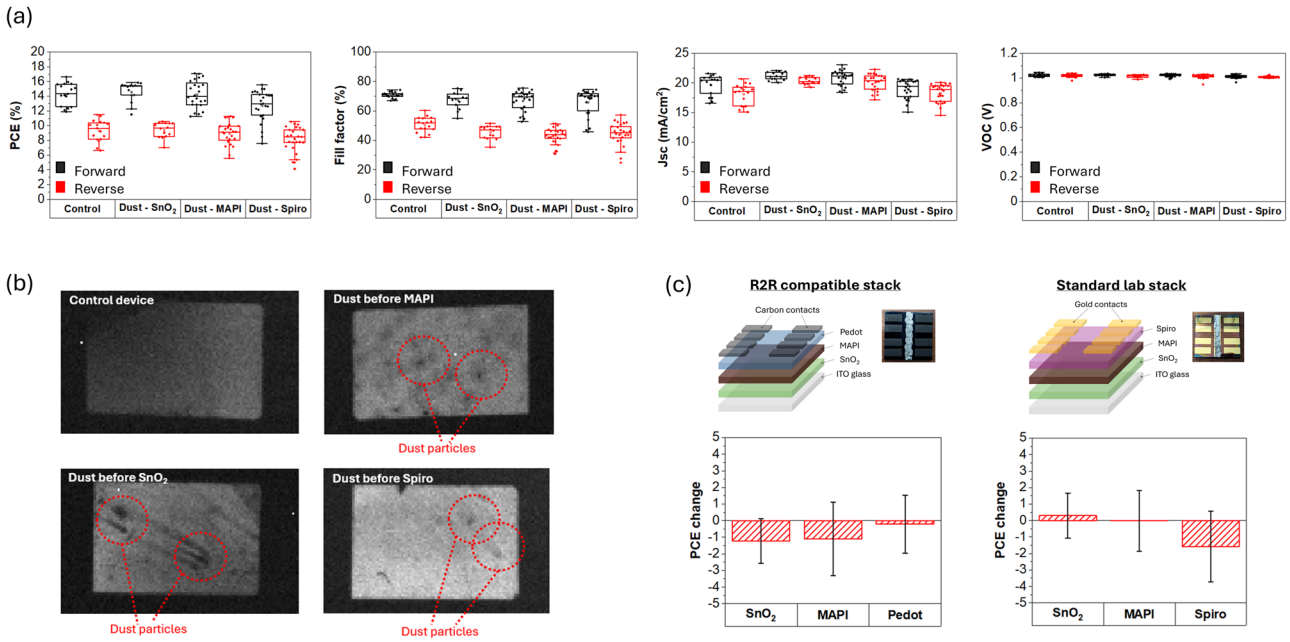

Fig. 7 | Device performance boxplots and EL mapping of standard lab stack control devices alongside three different device groups with dust – dust deposited before the ETL, perovskite and HTL layers, and percentage change in performance across all devices. a PCE, fill factor, Jsc and Voc box plots of control samples vs. those with dust deposited prior each to SnO_2, MAPI and spiro-MeOTAD; (**b**) EL maps of pixels from control samples vs. those with dust deposited prior each to SnO_2, MAPI and spiro-MeOTAD; (**c**) PCE change from controls in dusty device for both device stacks.

The ETL layer showed varying results across the two device stacks, with the R2R compatible stacks displaying more significant performance loss with dust at this layer, in particular J_{sc}, but less evidence of active area reduction in EL mapping. At the perovskite layer there were no changes to crystal size or shape were noted around particles. Instead, particles were more likely to cause changes to the microstructure (breakage or changes in topography). Some breakages were noted under SEM but very few. This suggests that the growth of perovskite crystals is resistant to the presence of inert dust particle in the size range of 1–10 µm, but the performance losses in the devices arise from the gaps created amongst the crystal microstructure reducing the active area. The R2R compatible stack showed less change in device performance when dust was deposited at the HTL layer, suggesting that the thicker PEDOT HTL and carbon top contact may be more resilient to dusty environments.

These findings go some way towards answering whether good quality planar perovskite solar cells can be made outside of a cleanroom environment, with results showing that even with many non-conductive dust particles present, devices can still perform well. This depends on the materials used, with spiro-MeOTAD and gold showing evidence of being more susceptible to reduced performance. These findings also suggest that at research level when making lab scale devices that a cleanroom may not be essential when it comes to devices and materials suitable for upscaling, and if it is required may not need to be much more than the lowest level of control for dust particles. With the emphasis towards creating low-cost options of renewable energy the potential ability to manufacture these solar cells in a non-cleanroom environment makes the process far more accessible where funds may be less abundant, and for better cost-effectiveness regarding upscaling to an industry level.

While this study provides a systematic assessment of dust effects on small-area perovskite solar cells, including R2R-compatible architectures, it does not extend to full module-scale devices. Evaluating the influence of particulate contamination on large-area modules (> 10 cm^2), where defect propagation and electrical interconnection losses may play a more critical role, is beyond the scope of this work and remains an important direction for future investigation.

This topic warrants further exploration, partly due to the wide variety of solar cells produced in cleanrooms but also considering different types of dust particles, potentially conductive or with other unique properties, could introduce new challenges for solar cell performance. Nevertheless, the promising results observed here highlight the resilience of planar perovskite solar cells, paving the way for more accessible and lower cost green energy.

Methods

Calculations

Dust particles dropout rate. This calculation approximates the amount of dust particles which will settle onto a certain area, depending on the number of particles present in the atmosphere.

Stokes law for small particles was required to first calculate dust particle settling velocity using the following equation:

$$v = \frac{2}{9}(d_1 - d_2)gr^2/\eta$$

where:

V = air viscosity of 1.8×10^{-5}

d_1 = particle density of 900 kg/m^3 (units adjusted from the test dust particle density 0.45 g/cm^2)

d_2 = air density of 1.204kg/m^3

g = gravitation constant 9.8 m/s^2

r = particle size of 1×10^{-6}m (1 µm)

This results in a settling velocity of 1.09×10^{-4}m/s or 3.91×10^{-2}mm/hr, further divided by 1000 for a dimensionless rate of 3.91×10^{-1}. This number is multiplied by the particle count, measured using an Airy Technology P311 particle counter (particles/m^3), giving an outcome describing the number of particles dropping out onto a m^2 surface which can then be converted to cm^2.

Hours of dust particle accumulation. The time taken for a surface of this size in different locations to accumulate the same amount of dust particles as are deposited in the dust box (T) is calculated using the actual

measured particle count in the dust box divided by the particle dropout rate in each location.

$$T = \text{Dust box particle count}/\text{Dropout rate}$$

Materials

Chemicals and solvents used in this study including lead iodide (PbI_2, TCI chemicals, 99.99%), methylammonium iodide (MAI: Greatcell Solar, >99% anhydrous), tin (iv) oxide colloidal dispersion liquid (Alfa Aesar, 15% in H_2O), PEDOT (HTL SOLAR3, Ossila), carbon black nanosize primary particles (Imerys, Ensaco), synthetic graphite (Imerys, Timrex), 1-butanol (Scientific Laboratory Supplies, 99.8% anhydrous), methylamine solution (Fisher Scientific, 33% in ethanol), and 2-methylanisole (Alfa Aesar, >99%) were purchased and used without further purifications or dilutions.

Additional chemicals and solvents used included Spiro-MeOTAD powder (high-performance liquid chromatography, 99%), lithium bis(trifluoromethylsulfonyl)imide salt (Li-TFSI, 99.99%), 4-*tert*-butylpyridine (t-BP, 96%), FK209 Co(iii) TFSI salt, ethyl cellulose, acetonitrile (99.8% anhydrous), and chlorobenzene (99.8% anhydrous), which were all purchased from Sigma-Aldrich.

Test dust used in this study was standardised household test dust ~90% by volume below 5 μm from Ellis Components.

Spin coating device fabrication

ITO glass substrates (sheet resistance $15\Omega sq^{-1}$) were cleaned by sonicating in a Hellmanex to de-ionised (DI) water ratio of 1:40 at 40 °C for 10 min, then rinsed with water. The samples were then sonicated in DI water, then acetone and finally IPA, all for 10 min each time and dried using a nitrogen gun. Surface treatment was UV-Ozone for 15 min to improve wetting ability and remove any remaining contaminants. For samples requiring dust circulation prior to ETL deposition, this was done after this point and before depositing the ETL.

For both stacks, the ETL layer was deposited by spin coating a diluted solution (4.2%wt SnO_2) of Tin (IV) Oxide colloidal dispersion (Alfa Aesar, 15% in H_2O) at 4000 rpm for 30 s, then annealed at 150 °C for 10 min. MAPI solution was then spin coated onto SnO_2 samples at 3000 rpm for 59 s, and annealed for 10 minutes at 120 °C.

For the HTL layer and top electrode of R2R compatible devices PEDOT (Solar 3 – Ossila) is used as received with no further changes or filtering required. Samples were spin coated at 3000 rpm for 40 s and annealed for 10 min at 110 °C. The carbon used for the top contacts on the R2R compatible devices uses the paste formula of 21.6% carbon black and a ratio of 2.6:1 graphite:carbon black, with Methylanisole as the solvent and 12.5% Ethyl Cellulose as the binder. Contacts were stencilled on using a mask to create eight top contacts, or pixels, then dried at 110 °C for 10 min.

For the HTL layer and top electrode on the standard lab devices, a solution of 90 mg ml^{-1} Spiro-MeOTAD in Chlorobenzene was spin coated at 3000 rpm for 40 s, then annealed at 110 °C for 10 min. Gold contacts were evaporated on at a thickness of ~100 nm.

For samples and devices with dust in, dust deposition was conducted prior to the spin coating of the specified layer, after the annealing of the previous layer. Samples were placed into the dust box, dust was circulated and samples were left until the particle counter reached zero. Clean control samples waited an equal amount of time before the next layer was deposited.

Characterisation

To measure photovoltaic performance on complete devices a Newport Oriel Sol3A was used in conjunction with a Keithley 2400 source metre. JV curves were measured at 1 sun, calibrated using a Newport KG5 Window reference cell. A 5 s light soaking was applied before each scan, and devices were measured at room temperature using a reverse scan (1.1 to −0.1 V) and forward scan (−0.1 V to 1.1 V) under a constant scan speed of $85mVs^{-1}$. The active area of all devices was defined by placing a 0.09 cm^2 mask on top of the device.

Optical microscopy was carried out using a Zeiss Primotech optical microscope at 10x zoom.

SEM images were obtained using a JEOL JSL 7800 F FEG scanning electron microscope (SEM). Dust samples were mounted onto conductive carbon stickies. All samples were sputter coated in 5 nm of gold palladium for improved conductivity. Samples were imaged using 10 kV of electron energy and images captured at varying magnifications. Chemical analyses of dust particles were carried out with an Oxford Instruments Ultim energy-dispersive x-ray spectroscopy (EDS) detector with AZTEC software (ver 6.0) analysis package at a 10 mm working distance.

Electroluminescence mapping was performed using an infrared camera setup to image the EL produced at the active area of devices while a voltage of 1.5 V was applied. Camera settings: exposure, 2×10^6 μs; gain, 30db.

XPS analysis and mapping were carried out using a Kratos axis supra XPS equipped with a minibeam 6-gas cluster ion source.

XRD scans used a Bruker D8 advance instrument with a copper source, in Bragg–Brentano geometry, between 10° and 50° with a 0.02° step size and time of 1 s per step. Repeat scans were done on each sample at 1 h after manufacture, 72 h after, 6 days, and 20 days.

Data availability

Data available upon request from the corresponding author.

Received: 27 March 2025; Accepted: 14 October 2025;
Published online: 24 November 2025

References

1. Ma, F. et al. Mechanism for improving kesterite solar cells performance via filed passivation effect induced by V-Doped MoSe2 interface layer at back Interface. *Sol. RRL* **7**, 2300042 (2023).
2. Pazos-Outón, L. M., Xiao, T. P. & Yablonovitch, E. Fundamental efficiency limit of lead iodide perovskite solar cells. *Am. Chem. Soc.* **9**, 1703–1711 (2018).
3. Jin, H. et al. It's a trap! On the nature of localised states and charge trapping in lead halide perovskites. *Mater. Horiz.* **7**, 397–410 (2020).
4. Johnston, M.B. & Herz, L.M. Hybrid perovskite for photovoltaics; charge-carrier recombination, diffusion and radiative efficiencies. *Acc. Chem. Res.* **49**, 146–154 (2015).
5. Yin, Y., Guo, Z., Chen, G., Zhang, H. & Yin, W. J. Recent progress in defect tolerance and defect passivation in halide perovskite solar cells. *Wuli Huaxue Xuebao/ Acta Phys. - Chim. Sin.* **37**, 1 (2021).
6. Kim, G. W. & Petrozza, A. Defect tolerance and Intolerance in Metal-Halide Perovskites. *Adv. Energy Mater.* **10**, 2001959 (2020).
7. Min, J., Choi, Y., Kim, D. & Park, T. Beyond imperfections: exploring defects for breakthroughs in perovskite solar cell research. *Adv. Energy Mater.* **14**, 1 (2024).
8. Zheng, D., Raffin, F., Volovitch, P. & Pauporté, T. Control of perovskite film crystallization and growth direction to targt homogenous monolithic structures. *Nat. Commun.* **13**, 1 (2022).
9. Barua, P. & Hwang, I. Bulk Perovskite crystal properties determined by heterogeneous nucleation and growth. *Materials* **16**, 2110 (2023).
10. Adhyaksa, G. W. P. et al. Understanding detrimental and beneficial grain boundary effects in halide perovskites. *Adv. Mater.* **30**, 1804792 (2018).
11. Adhyaksa, G. W. P. Understanding the impacts of grain size variation, distribution, and recombination losses in halide perovskites: a generalized semi-analytical model from thin-film to photovoltaics. *Energy Technol.* **10**, 2200011 (2022).
12. Nukunudompanich, M., Budiutama, G., Suzuki, K., Hasegawa, K. & Ihara, M. Dominant effect of the grain size of the MAPbI3perovskite controlled by the surface roughness of TiO2on the performance of perovskite solar cells. *CrystEngComm* **22**, 2718–2727 (2020).

13. Ni, Z., Xu, S. & Huang, J. Response to Comment on "Resolving spatial and energetic distributions of trap states in metal halide perovskite solar cells, *Science* **371**, 1352 (2021).
14. Holzhey, P., Prettl, M., Collavini, S., Mortan, C. & Saliba, M. Understanding the impact of surface roughness: changing from FTO to ITO to PEN/ITO for flexible perovskite solar cells.*Sci. Rep.***13**, 6375 (2023).
15. Agarwal, S. & Nair, P. R. Pinhole induced efficiency variation in perovskite solar cells. *J. Appl Phys.* **122**, 163104 (2017).
16. Ono, L. K. et al. Pinhole-free hole transport layers significantly improve the stability of MAPbI3-based perovskite solar cells under operating conditions. *J. Mater. Chem. A Mater.* **3**, 15451–15456 (2015).
17. Bowling, A. Single-wafer processing and real-time process conctrol for semiconductor integrated circuit manufacturing. *Solid State Technol.* **37**, 45 (1994).
18. Hattori, T. Consequences of spatial distributions of the interface states on the Schottky barrier. *Solid State Technol.* **33**, S1–S9 (1990).
19. Imafuku, D. et al. Organic contmaination of silicon wafer in clean room air and its impact to gate oxide integrity. *Mater. Res. Soc. Symp. Proc.* **473**, 161 (1997).
20. Zhao, W., Li, H. & Wang, S. Energy performance and energy conservation technologies for high-tech cleanrooms: State of the art and future perspectives. *Renew. Sustain. Energy Rev.* **183**, 113532 (2023).
21. Mohd Asri, M. A., Nordin, A. N. & Ramli, N. Low-cost and cleanroom-free prototyping of microfluidic and electrochemical biosensors: techniques in fabrication and bioconjugation. *Biomicrofluidics* **15**, 061502 (2021).
22. Walsh, D. I., Kong, D. S., Murthy, S. K. & Carr, P. A. Enabling Microfluidics: from Clean Rooms to Makerspaces. *Trends Biotechnol.* **35**, 383–392 (2017).
23. Kumar, T., Owyeung, R. E. & Sonkusale, S. R. Rapid cleanroom-free fabrication of thread based transistors using three-dimensional stencil-based patterning. *Flex. Print. Electron.* **6**, 015007 (2021).
24. Beynon, D. et al. All-printed roll-to-roll perovskite photovoltaics enabled by solution-processed carbon electrode. *Adv. Mater.* **35**, 2208561 (2023).
25. Parvazian, E. & Watson, T. The roll-to-roll revolution to tackle the industrial leap for perovskite solar cells. *Nat. Commun.* **15**, 1 (2024).

Acknowledgements

This work was made possible by the funding supplied by the STRIP5 Prosperity Partnership [EP/X025217/1]. Additional support was received from the SPECIFIC Innovation and Knowledge Centre by the Engineering and Physical Science Research Council Programme Grant ATIP (Application Targeted and Integrated Photovoltaics) [EP/T028513/1], and the Advanced Imaging of Materials (AIM) facility at Swansea University which was funded in part by the EPSRC [EP/M028267/1].

Author contributions

Kathryn Lacey: writing original draft, conceptualisation, methodology, validation, investigation, formal analysis, visualisation. Ershad Parvazian: writing original draft, conceptualisation, methodology, validation, investigation, formal analysis, visualisation. Sarah-Jane Potts: formal analysis. Tom Dunlop, James McGettrick: formal analysis. Eifion Jewell: methodology, formal analysis. Krishna Senuarine: methodology. Matt Carnie: resources. Matthew Davies: resources. Trystan Watson: supervision, resources, conceptualisations, validation.

Competing interests

The authors declare no competing interests.

Additional information

Supplementary information The online version contains supplementary material available at https://doi.org/10.1038/s43246-025-00993-y.

Correspondence and requests for materials should be addressed to Trystan Watson.

Peer review information *Communications Materials* thanks Cheng Liu and the other, anonymous, reviewer(s) for their contribution to the peer review of this work. A peer review file is available.